THE JOURNAL OF
PHYSICAL
CHEMISTRY
C
A JOURNAL OF THE AMERICAN CHEMICAL SOCIETY

February 9, 2023
Volume 127
Number 5
pubs.acs.org/JPCC

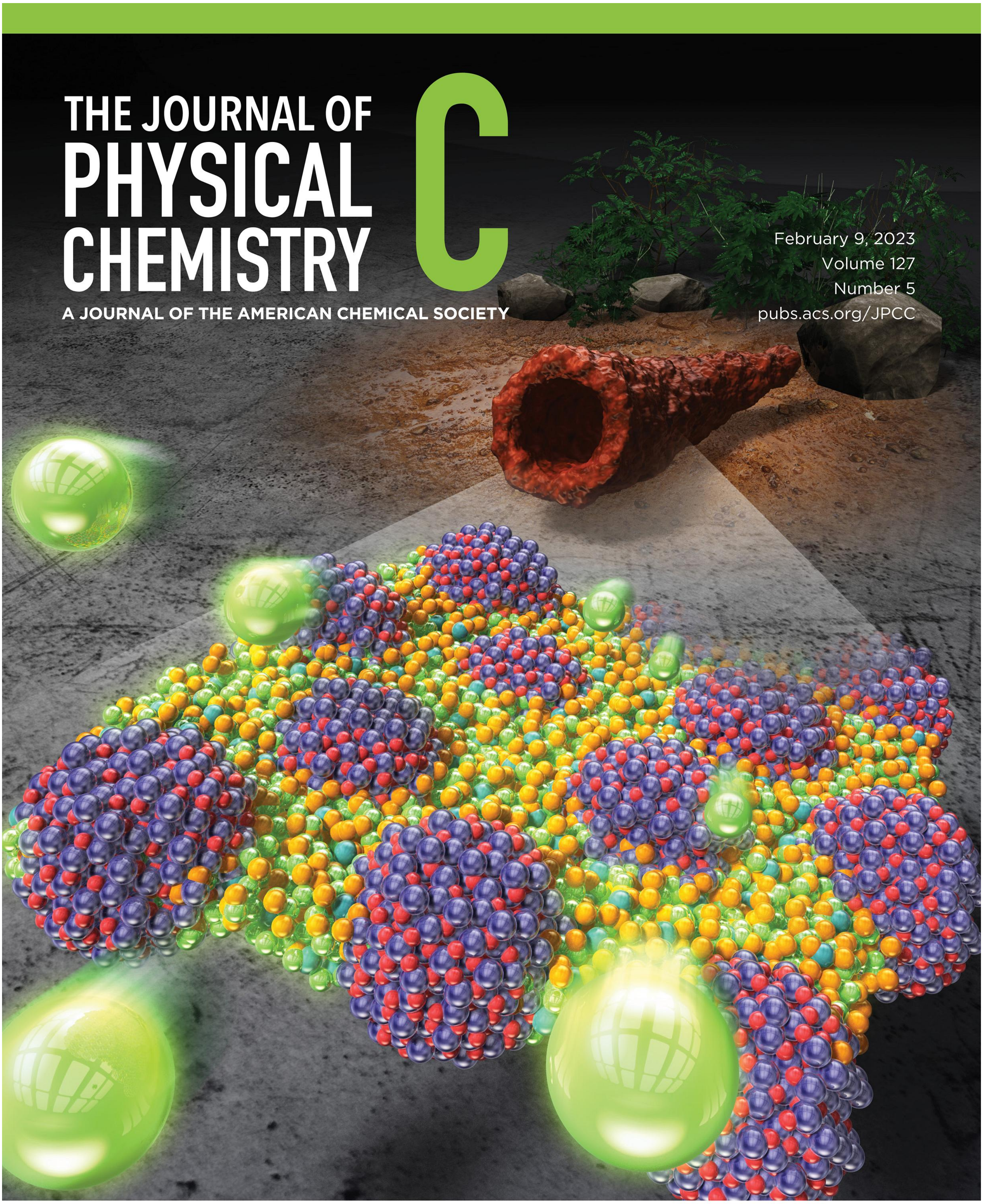

ACS Publications
Most Trusted. Most Cited. Most Read.

www.acs.org

Uniform Formation of Characteristic Nanocomposite Structure of Biogenous Iron Oxide for High-Rate performance as Anode of Lithium-Ion Battery

Masakuni Takahashi[†], Ryo Sakuma[†], Hideki Hashimoto[†], Tatsuo Fujii[†,*], Jun Takada[†]

[†] *Graduate School of Natural Science and Technology, Okayama University, Okayama 700-8530, Japan.*

* Corresponding author (Email: tfujii@cc.okayama-u.ac.jp)

Abstract

Recently, Fe_2O_3 has been considered as an alternative anode material for lithium-ion batteries (LIBs) owing to its high theoretical capacity (approximately 1000 mAh g^{-1}), low cost, and nontoxicity. However, its rate performance remains poor relative to that of the conventional graphite anode. In this study, Fe_2O_3-based anodes were prepared through the annealing of biogenous Fe_2O_3 (*L*-BIOX) samples produced by an aquatic Fe-oxidizing bacteria. The effect of the annealing temperature on the performance of the synthesized Fe_2O_3-based material as the anode of an LIB was investigated. Electrochemical measurements revealed that the annealed *L*-BIOX samples at 300–700 °C exhibited higher rate performances than the unannealed material. Particularly, the sample annealed at 700 °C exhibited the highest capacity among the synthesized materials and showed a higher performance than those of the previously reported Fe_2O_3-based anodes. It exhibited a capacity of 923 mAh g^{-1} even at a high current density of 2 A g^{-1}. After annealing at 700 °C and discharging, the synthesized biogenous material had a uniform nanocomposite structure composed of α-Fe_2O_3 nanoparticles dispersed in an amorphous matrix of Li–Si–P oxide. To form this uniform nanostructure reduced the solid-state diffusion resistance of the Li^+ ions in the active material, which consequently improved the rate performance of the electrode. Therefore, this study provides substantial insights to the development and improvement of the performance of novel Fe_2O_3-based nanomaterials as the anode of LIBs.

KEYWORDS : high rate, biogenous iron oxide, nanocomposite structure, conversion anodes, lithium ion battery.

Introduction

Lithium-ion batteries (LIBs) have been used as power sources for portable electronics and electric vehicles.[1–4] Owing to their high energy densities, LIBs are also considered as potential energy devices in grid-level energy storage applications. For applying to these applications, LIBs require to further improve the battery performance. LIBs are mainly composed of an anode, a cathode, a nonaqueous electrolyte, and a separator.[5] Among these components, the active materials on the anode and cathode directly influence the capacity and rate performance of the battery.[4,6] Carbon-based materials, such as graphene, activated carbon, and graphite, are among the best-performing anode active materials.[7,8] Particularly, graphite is the most widely used anode for LIBs owing to its low cost, low electrochemical potential against the Li^+/Li electrode (0.2 V), and good charge–discharge properties.[9,10] However, commercially available graphite-based electrodes have already reached the specific theoretical capacity (372 mAh g^{-1}).[9,11] Therefore, the development of alternative anode materials with high capacities, good rate capabilities, and excellent cycling stabilities is important to further improve the performance of LIBs.

Recently, Fe_2O_3 has attracted considerable research attention and has been developed as the active anode material for LIBs owing to its high theoretical capacity (approximately 1000 mAh g^{-1}), low cost, and nontoxicity.[12,13] However, the cycle and rate performances of bulk Fe_2O_3 does not measure up to those of the conventional anode materials, because bulk Fe_2O_3 occur the chemo-mechanical breakage by large volume change during charge-discharge process and show low conductivity.[12,13] To improve the electrochemical storage properties, nanostructured Fe_2O_3 have been used instead of bulk Fe_2O_3. Similarly, the morphology of Fe_2O_3 can be engineered to enhance its rate performance.[14–23] For instance, spindle-like mesoporous α-Fe_2O_3 and hierarchical flower-like mesoporous Fe_2O_3 nanosheets exhibited excellent rate performances; at a high current density of 2 A g^{-1}, the discharge capacities recorded were approximately 780 and 910 mAh g^{-1}, respectively.

These were much higher than that of the bulk Fe_2O_3 (approximately 500 mAh g^{-1}).[17,20,23] Therefore, the design of new Fe_2O_3 nanostructures is a feasible approach to improve its performance as an anode material for LIBs.

In our previous studies, biogenous Fe_2O_3 (*L*-BIOX) produced by an aquatic Fe-oxidizing bacteria, *Leptothrix ochracea*, showed a better rate and cycle performance than its bulk counterpart owing to a characteristic nanocomposite structure, which formed during the first discharging step.[24,25] *L*-BIOX was composed of Fe, Si, and P in a molar ratio of 73:22:5. It exhibited a microcylindrical morphology and a hierarchical structure composed of amorphous nanoparticles with an average diameter of 3 nm.[26] During the initial discharge process, the amorphous structure of *L*-BIOX changed into a nanocomposite structure consisting of dispersed Fe nanoparticles with an average diameter of 2 nm in an amorphous Li–Si–P oxide matrix.[24] Therefore, the high rate performance of *L*-BIOX was possibly due to this unique nanocomposite structure, which provided conduction paths for the transfer of Li^+ ions during the charge–discharge processes.[24] In other previous study, the annealing of *L*-BIOX caused to remove a water in the material, thereby reducing irreversible capacity and improving cycle performance.[27] In addition, nanocomposite P containing iron oxide/Si oxide nanocomposite structure was also produced after the annealing of the biogenous *L*-BIOX sample.[28,29]

Considering the merits of these previous studies, the nanocomposite structure of *L*-BIOX and its structural modification by annealing caused to improve and optimize its rate performance as the anode of LIBs. In this study, *L*-BIOX annealed at various temperatures was reviewed for further optimization of its nanocomposite structure to improve its rate performance. In addition, the charge transfer resistance and solid-state diffusion resistance of the Li^+ ions in the active material were evaluated using electrochemical impedance spectroscopy (EIS) measurements and cyclic voltammetry. From these results, the effect of the nanocomposite structure of the unannealed and annealed *L*-BIOX electrodes on the rate performance was studied.

Experiment

Preparation and characterization of the *L*-BIOX samples

The *L*-BIOX samples were collected from a water-purifying tank at the Okayama University, Japan. Thereafter, the samples were uniformly dispersed in H_2O. The pH of the suspension was adjusted to 10.5 by adding NH_4OH(28%, Nacalai Tesque, Japan). The suspension was left to stand for 40 min, and the settled powder was removed. Subsequently, the dispersed *L*-BIOX particles in the solution were collected through suction filtration and washed using ion-exchanged water. The collected *L*-BIOX samples were dried at 100 °C for overnight and then annealed at 300–900 °C for 2 h in air at 10 °C min^{-1}.

The crystal structures of the samples were evaluated through X-ray diffraction (XRD) measurements using a RINT-2000 (Rigaku, Japan) diffractometer with a Cu–Kα radiation (λ = 0.154 nm). The morphologies of the samples were determined through the scanning transmission electron microscopy (STEM) and the high-angle annular dark-field scanning transmission electron microscopy (HAADF-STEM) with a CEOS CS-corrector (JEM-2100F, JEOL, Japan). Lastly, the chemical bonding states were evaluated through Fourier transform infrared (FT-IR) analysis (Nicolet 6700, Thermo Scientific, USA).

Electrochemical measurements

A slurry was prepared by mixing 70 wt% the *L*-BIOX active material, 14 wt% Ketjenblack ECP, 6 wt% vapor grown carbon fibers, and 10 wt% KF polymer in an appropriate amount of N-methyl-

2-pyrolidone. The slurry was applied on Cu foil substrates using doctor blade method. Thereafter, the coated Cu substrates were dried at 120 °C for 30 min in a vacuum to form the anode. The dried anode was punched and roll-pressed to have a 16 mm diameter. Thereafter, a coin cell was assembled using the *L*-BIOX-coated Cu substrate, a metal Li foil, and a fiber filter paper as the anode, counter electrode, and separator, respectively. The electrolyte used was 1 M $LiPF_6$ in an ethylene carbonate/dimethyl carbonate solution with a volume ratio of 3:7. The cycle characteristics of the samples were evaluated through 30 cycles of galvanostatic charge–discharge (GCD) tests from 0.01–3 V at a current density of 0.6 A g^{-1}. The rate characteristics were evaluated through 5 cycles of GCD measurements from 0.01–3 V at current densities from 0.1 to 2 A g^{-1}. Lastly, EIS measurements were recorded from 7.0 MHz to 0.1 Hz with an amplitude of 10 mV at open circuit volage before and after 1st or 5th cycles of GCD measurements from 0.01–3 V at a current density of 0.1 A g^{-1}. The cyclic voltammetry was carried out using a three-electrode cell at room temperature. The three-electrode cell was assembled using *L*-BIOX-coated Cu substrate, metal Li foil, a fiber filter paper, and 1 M $LiPF_6$ in an ethylene carbonate/dimethyl carbonate solution (volume ratio of 3:7) as the anode, counter and reference electrodes, separator, and electrolyte, respectively. The cyclic voltammetry was performed from 0.01–3 V at scan rate from 0.2 to 1.0 mV s^{-1}.

Results and discussion

First, we describe the previous results reported on the effect of annealing temperature on the structure and morphology of *L*-BIOX.[29] Figure 1(a) shows the XRD patterns of the unannealed and annealed *L*-BIOX samples at various temperatures. The broad peaks at $2\theta = 34°$ and $62°$ observed in the XRD patterns of the unannealed and annealed *L*-BIOX samples at 300 and 500 °C can be well indexed to amorphous Fe oxyhydroxide.[30] The intensities of these broad peaks increased with the increasing annealing temperature. Apart from the peaks corresponding to Fe oxyhydroxide, weak diffraction peaks attributable to α-Fe_2O_3 were also observed in the XRD spectrum of the sample annealed at 700 °C. However, the diffraction peaks observed in the XRD spectrum of the sample annealed at 800 °C correspond only to α-Fe_2O_3. No diffraction peaks attributed to other phases, such as Si and P oxides, were observed in the XRD spectra of all the *L*-BIOX samples. These results suggest that the crystallization of the *L*-BIOX sample to α-Fe_2O_3 progressed at 700-800 °C. This temperature is higher than the crystallization temperature to α-Fe_2O_3 of the common iron oxyhydroxides, which is 200-340 °C. The high crystallization temperature of *L*-BIOX originated from that Si and P in *L*-BIOX suppress by ion rearrangement during the annealing process.

Figure 1(b) shows the FT-IR spectra of the unannealed and annealed *L*-BIOX samples at various temperatures. The peaks at approximately 1000, 1620, and 3400 cm^{-1}, which can be attributed to the stretching mode of Si–O–Fe and P–O–Fe bonds and the bending and stretching modes of the O–H bond, respectively, were observed in the FT-IR spectrum of the unannealed sample.[30–33] The peaks corresponding to the O–H bond were observed owing to the adsorption of –OH groups and H_2O molecules on the sample surface. The peak at approximately 1000 cm^{-1} shifted toward higher wave numbers with the increasing annealing temperature. For instance, after annealing at 800 °C, this peak was recorded at 1100 cm^{-1}, which could be attributed to the stretching mode of the Si–O–Si bond in SiO_2.[34] Therefore, it revealed that the phase separation of Fe oxide and Si oxide proceeded with increase of annealing temperature.

Figure 1(c)–(g) show the STEM images of the unannealed and annealed *L*-BIOX samples at various temperatures. The unannealed and the annealed *L*-BIOX samples at 300–700 °C had porous, nanofiber morphologies [Figure 1(c)–(f)]. In contrast, the nanofiber structure was retained after annealing at 800 °C although the nanofibers aggregated [Figure 1(g)]. Furthermore, the *L*-BIOX sample produced at this annealing temperature had a small pore structure. To investigate further the changes in the morphology of the samples after annealing, the HAADF-STEM images of the unannealed and annealed *L*-BIOX samples at various temperatures are shown in Figure 1(h)–(l). Figure 1(h) confirms that the unannealed *L*-BIOX nanofibers were composed of interconnected nanoparticles. The *L*-BIOX samples annealed at 300–800 ℃ exhibited nanocomposite structures composed of bright primary particles embedded in dark matrices [Figure 1(i)–(l)]. The size of the bright primary particles increased with the increasing annealing temperature. From the FT-IR and XRD results, the bright primary particles and the dark matrix observed in the annealed *L*-BIOX samples at 300–800 ℃ were possibly the iron oxide and amorphous Si oxide phases, respectively. In the previous study of our group[29], the P *K*-edge X-ray absorption near edge structure spectra of both pristine and annealed *L*-BIOX had the same profiles as $FePO_4 \cdot 4H_2O$ regardless of the annealing temperature. It is considered that P is not phase-separated by annealing. It is considered that P is not phase-separated by annealing and exists in solid solution in iron oxide. Therefore, during annealing, phase separation proceeded to form the nanocomposite structure comprising the dispersed P containing iron oxide nanoparticles in the amorphous Si oxide matrix.

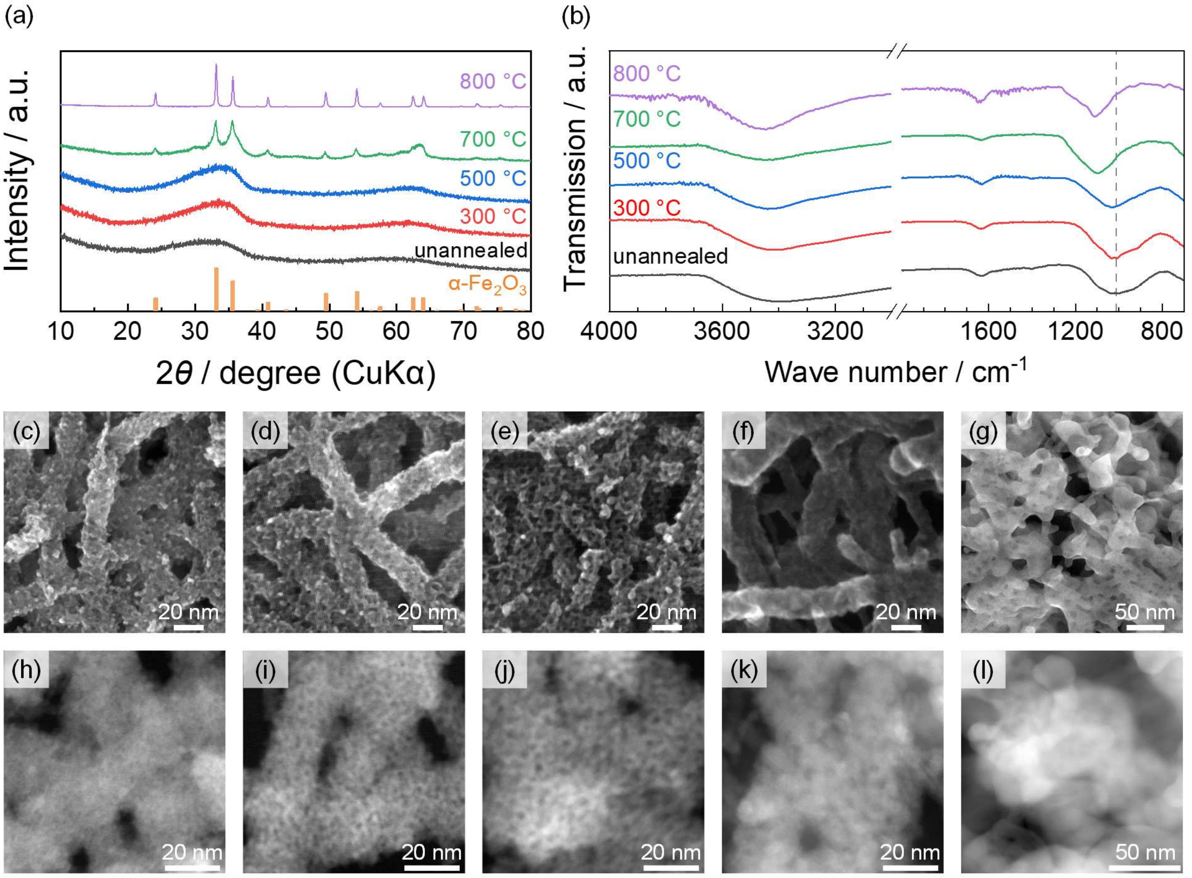

Figure 1. (a) XRD patterns and (b) FT-IR spectra of *L*-BIOX annealed at various temperatures for 2 hours. (c)-(g) STEM images and (h)-(l) HAADF-STEM images of *L*-BIOX annealed at various temperatures for 2 hours. (c) and (h), (d) and (i), (e) and (j), (f) and (k), (g) and (l) represent the unannealed, 300, 500, 700, 800 °C of annealing temperature, respectively. These results were reported at 2015 Elsevier.[29]

Figure 2(a) shows the first discharge–charge voltage profiles of the *L*-BIOX samples measured from 0.01–3.0 V at a current density of 0.1 A g^{-1}. Voltage plateaus at approximately 0.8 and 1.5 V were observed in the discharge curves of all the samples. The voltage plateau observed at approximately 0.8 V corresponds to the transformation of the Fe^{2+} ions to Fe^0 .[13,17] In addition, when Si was doped into ferrihydrite, the transformation of the Fe^{3+} ions to Fe^{2+} ions reduction reaction occurred at approximately 1.5 V.[35,36] The first discharge capacities of the unannealed and annealed *L*-BIOX samples at 300, 500, 700, 750, 800 and 900 °C were 1427, 1521, 1546, 1493, 1421, 1336 and 1055 mAh g^{-1}, respectively. Correspondingly, the first charge capacities were 964, 1041, 1075, 1040, 970, 886 and 710 mAh g^{-1}. The loss of capacity between the charge/discharge processes in the *L*-BIOX annealed at 700 °C or less was lower than that of unannealed *L*-BIOX. The observed loss of capacity between the charge/discharge processes is possibly due to the irreversible storage to form the Li–Si–P oxide matrix[24,35,36] and a solid electrolyte interphase (SEI) layer at the electrode/electrolyte interface.[13] The solid solution of Si and P in iron oxide was phase-separated during the charge-discharge process to form the Si–P amorphous oxide matrix. At the same time, Li$^+$ ions irreversibly stored in that oxide matrix, resulting in irreversible capacity. [24,35,36] It is reported in previous study that the adsorbed water on the surface increased irreversible capacity derived from the SEI formation.[27] Therefore, the irreversible capacity decreased by annealing at low temperature due to the removal of adsorbed water on the surface. The experimental reversible capacities of the samples exceeded the theoretical capacity. Moreover, the capacity of samples increased with increase of annealing temperature from 300 to 500 °C, while it decreased with increase of annealing temperature above 700 °C (Figure S1). The observation of exceeded the theoretical capacity corresponds well to those of the previous reports on Fe_2O_3-based anode materials.[37–41] The experimental capacity was higher than the theoretical value because of the storage of Li$^+$ ions on the surface and kinks of α-Fe_2O_3, which were not accounted for in the theoretical calculations.[39,41] The decrease of capacity when the *L*-BIOX annealed at over 700 °C is due to the particle enlargement. From HADDF-STEM images, the rapidly enlargement of iron oxide in *L*-BIOX was observed in case of the *L*-BIOX annealed at 800 °C. In addition, the STEM and HAADF-STEM images of the *L*-BIOX annealed at 900 °C shown in Figure S2 revealed that the particle size of α-Fe_2O_3 in the *L*-BIOX annealed at 900 °C is about 10 times larger than that at 800 °C. The enlargement of the particles reduced a surface area, resulting the decrease of the storage of Li^+ ions on the surface and kinks. Therefore, the capacity is considered to have dramatically decreased when annealing at over 700 °C.

Figure 2(b) shows the cycle performances of the unannealed and annealed *L*-BIOX samples at various temperatures evaluated through GCD tests from 0.01–3.0 V at a current density of 0.6 A g^{-1}. Figure S3 shows the discharge–charge profiles of the samples. The discharge capacities of the samples unannealed and annealed at 300-800 °C were >90% even after 30 cycles of GCD tests. In addition, some samples showed the higher capacity at 30th cycle test than that of 2nd cycle. On the other hand, the capacity of the *L*-BIOX annealed at 900 °C decreased with increase of a number of GCD test. During the discharge–charge processes, α-Fe_2O_3 typically undergoes a large volume change. This led to the chemo-mechanical breakage of the electrode material, which reduces the electrical contact between the active material and the current collector.[38,42] However, pores in the anode materials can suppress the chemo-mechanical destruction of the active material, thereby mitigating the effects of the volume expansion of α-Fe_2O_3.[22,39] Therefore, the capacities of the samples unannealed and annealed at 300-800 °C were well maintained owing to their porous structures as observed in the STEM images. In other side, the STEM and HAADF-STEM images of the *L*-BIOX annealed at 900 °C as shown in Figure S2 revealed that the porous structure was disappeared. As a result, the degradation due to volume expansion could not be suppressed, and the battery capacity decreased with a number of GCD tests. The tendency of increasing capacity with increase of a number of cycles has been reported in a number of metal oxide anode in LIBs.[43–46] The reasons of increasing capacity are improving utilization of the conversion reaction[47,48], optimization of the electrolyte-derived surface layer[49,50], and changes in morphology.[43] The reason of increased capacity with increasing number of cycles in this study may also be related to these factors, but it is difficult to determine the factors in this study.

Figure 2(c) shows the rate performances of the unannealed and annealed *L*-BIOX samples at various temperatures evaluated through GCD measurements from 0.01–3.0 V at current densities from 0.1 to 2 A g^{-1}; GCD profiles of the all samples are shown in Figure S4. The *L*-BIOX samples annealed at 300–700 ºC showed a higher rate performance than the unannealed sample; the rate performance increased with the increasing annealing temperature. In contrast, the sample produced after the annealing at over 750 °C exhibited a lower rate performance than that of 700 °C. Among the tested samples, the *L*-BIOX annealed at 700 °C showed the best rate performance. As the particle size of the anode material decreases, the rate performance improves owing to the shortening of the diffusion distance of the Li^+ ions.[13,42] Therefore, the sample annealed at over 750 °C had a poor rate performance because of its large particle size. However, the rate performance of the samples annealed at 300–700 ºC improved even though their particle size increased with the increasing annealing temperature. In these samples, nanocomposite structures were formed after annealing, as observed from the HADDF-STEM images. Therefore, the improvement in the rate performance of the annealed samples at 300–700 ºC is possibly due to the formation of the nanocomposite. Table 1 summarizes the capacities at 0.1 and 2.0 A g^{-1} and the capacity retention of the *L*-BIOX sample annealed at 700 ºC and of previously reported Fe_2O_3-based anode materials. At 2.0 A g^{-1}, the *L*-BIOX sample exhibited a higher capacity than the bulk and spindle-like mesoporous Fe_2O_3 materials and a comparable performance to that of the hierarchical flower-like Fe_2O_3 mesoporous nanosheets. Additionally, the capacity retention on the *L*-BIOX annealed at 700 ºC was higher than those on the previously reported Fe_2O_3-based anode materials. These observations reveal the higher performance of the *L*-BIOX sample synthesized in this study than those of the previously reported Fe_2O_3-based anode materials.

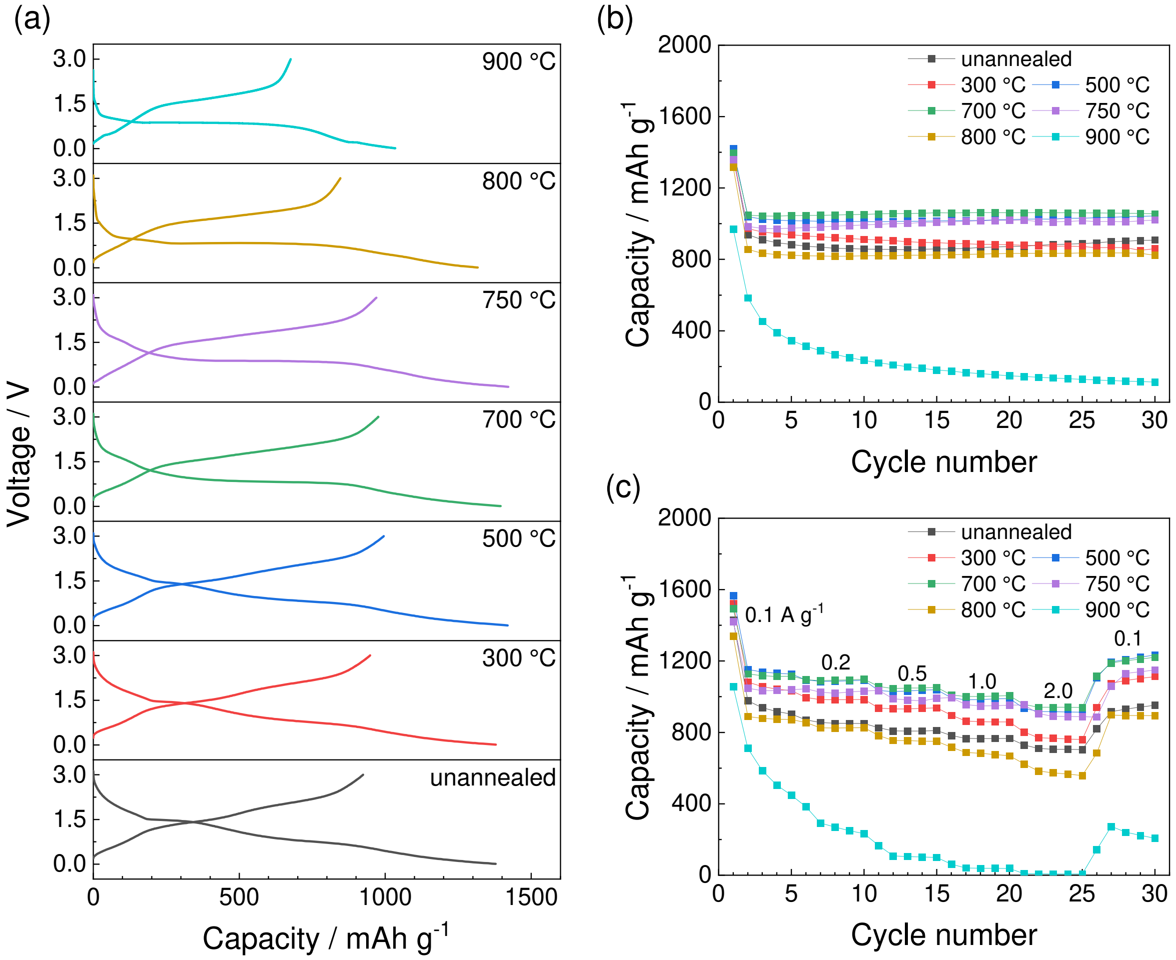

Figure 2. (a) First discharge/charge voltage profiles at a current density of 0.1 A g^{-1}, (b) cyclic performances at a current density of 0.6 A g^{-1} and (c) rate performances of the *L*-BIOX unannealed and annealed at various temperature.

Table 1. Capacities at 0.1 A g^{-1} and 2.0 A g^{-1} and the capacity retention of bulk Fe_2O_3, spindle-like mesoporous α-Fe_2O_3[23], hierarchical flower-like Fe_2O_3 mesoporous nanosheets[17] and *L*-BIOX annealed at 700 °C.

	Capacity / mAh g^{-1}		Capacity retention / %
	at 0.1 A g^{-1}	at 2.0 A g^{-1}	
Fe_2O_3 (bulk)[23]	893	500	56.0
spindle-like mesoporous α-Fe_2O_3 [23]	993	780	78.5
hierarchical flower-like Fe_2O_3 mesoporous nanosheets[17]	1970	910	46.2
L-BIOX annealed at 700 °C	1055	923	87.5

The charge transfer and solid-state diffusion resistances of the Li^+ ions in the active material, which are factors that determine the rate performance,[51–53] were then evaluated using EIS measurement and cyclic voltammetry. Figure S5 showed the Nyquist plots of the *L*-BIOX unannealed and annealed at 700 and 900 °C before and after 1st and 5th cycles of GCD measurements from 0.01–3.0 V at a current density of 0.1 A g^{-1}. Figure 3 shows the summary of Nyquist plots of the unannealed and annealed *L*-BIOX samples at 700 and 900 °C recorded by EIS measurements after 5 cycles of GCD measurements. Semicircles in the high- and medium-frequency regions and a line in the low-frequency region were observed in the Nyquist plots of the *L*-BIOX samples annealed at 700 and 900 °C. In contrast, for the unannealed *L*-BIOX sample, the straight line recorded in the low-frequency region was composed of two connected straight lines. The semicircles observed in the high- and medium-frequency regions can be attributed to the charge-transfer impedance on the SEI layer (R_{SEI}) and on the electrode–electrolyte interface (R_{ct}), respectively.[54] The line obtained in the low-frequency region corresponds to the Warburg impedance. From shape of these lines, it suggested that there were two diffusion paths in the unannealed *L*-BIOX sample, whereas only one was observed in the sample annealed at 700 and 900 °C.[55] The charge-transfer resistance at OCV state of unannealed *L*-BIOX was higher than that of annealed at 700 and 900 °C. In addition, the charge-transfer resistances of these samples reduced after 1st cycle and then increased after 5th cycles. The charge-transfer resistance at OCV state of *L*-BIOX annealed at 700 and 900 °C was lower than that of unannealed *L*-BIOX. The reason is the formation of α-Fe_2O_3, which exhibits higher electronic conductivity than amorphous iron oxide. The charge-transfer resistances at the 1st and 5th cycles were similar for the *L*-BIOX unannealed and annealed at 700 °C. In other hand, the charge-transfer resistances of *L*-BIOX annealed at 900 °C at the 1st and 5th cycles were higher than that of unannealed. To quantitatively evaluate charge transfer resistance of these samples, fitting impedance spectrum at 5th cycles was performed. Figure S5 (a) shows the equivalent circuit diagrams of the impedance spectra of these samples. The fitting results are shown in Figure S5 (b) - (d). Table 2 summarizes the obtained R_{SEI} and R_{ct} values. The R_{SEI} and the R_{ct} of the annealed sample at 700 and 900 °C were smaller and larger than those of the unannealed *L*-BIOX material, respectively. The particle size of the *L*-BIOX sample increased after annealing, which decreased the surface area of the active material. Consequently, the area of the SEI layer and the contact area between the electrolyte and the active material decreased, leading to the observed decrease in the R_{SEI} and increase in the R_{ct} values of the *L*-BIOX sample with increase of annealing temperature. The *L*-BIOX sample annealed at 700 °C showed a better rate performance even though its whole charge-transfer resistance was larger than that of the unannealed sample. From this, the improvement in the rate performance was not due to the enhancement of the charge transfer characteristics in the electrode interface.

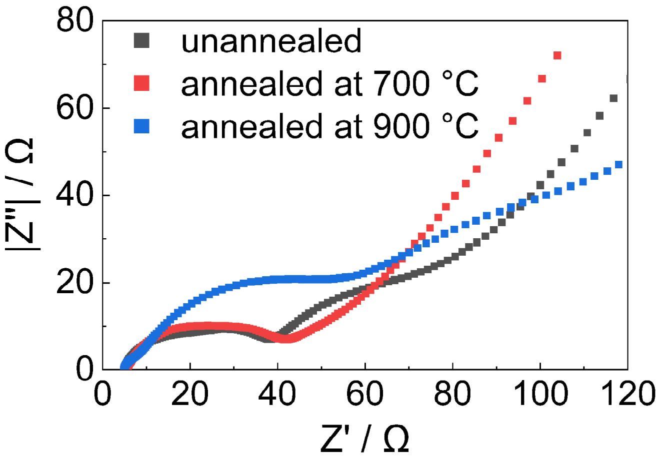

Figure 3. Nyquist plots of the *L*-BIOX unannealed and annealed at 700 °C after 5 cycles of GCD measurements from 0.01–3.0 V at a current density of 0.1 A g^{-1}.

Table 2. Impedance parameters of the *L*-BIOX unannealed and annealed at 700 °C after 5 cycles of GCD measurements from 0.01–3.0 V at a current density of 0.1 A g^{-1}.

	R_{SEI} / Ω	R_{ct} / Ω	$R_{SEI} + R_{ct}$ / Ω
unannealed	14.2	17.2	31.4
annealed at 700 ℃	7.2	26.5	33.7
annealed at 900 ℃	2.3	61.3	63.6

Accordingly, the diffusion coefficient of the Li^+ ions in the active materials were then evaluated by cyclic voltammetry. Figure 4 (a)-(c) was shown cyclic voltammograms from 0.01–3 V vs. Li^+/Li at scan rate from 0.2 to 1.0 mV s^{-1} for the *L*-BIOX unannealed and annealed at 700 and 900 °C. In these samples, anodic peaks were observed at approximately 1.6 V and 1.8 V corresponding to the transformation of the Fe^0 to Fe^{2+} and Fe^{2+} to Fe^{3+}.[56] In addition, cathodic peaks were observed at approximately 0.7 V and 1.4 V corresponds to the transformation of the

Fe^{3+} ions to Fe^0,[13,17] and the transformation of the Fe^{3+} ions to Fe^{2+} reduction reaction in Si doped ferrihydrite, respectively.[35,36] Currents of these peaks were increased with increase of scan rate. The linear relationship between current of the anodic peak at approximately 1.6 V and the square root of the scan rates was obtained, as shown in Figure 4(d). Then, the diffusion coefficients of *L*-BIOX unannealed and annealed at 700 and 900 °C calculated from these slopes were 5.72×10^{-11} $cm^2\ s^{-1}$, 1.99×10^{-10} $cm^2\ s^{-1}$ and 2.69×10^{-11} $cm^2\ s^{-1}$, respectively. The diffusion coefficient of the *L*-BIOX annealed at 900 °C was 2.12 times lower than that of unannealed. In other side, the diffusion coefficient of *L*-BIOX annealed at 700 °C was 3.48 times higher than that of unannealed. The low diffusion coefficient of the *L*-BIOX annealed at 900 °C was caused by increasing diffusion distance resulting from the significant particle growth by annealing at high temperature. The fast diffusion of the Li^+ ions in the *L*-BIOX annealed at 700 °C can be attributed to the uniform formation of nanocomposite structure composed of the dispersed Fe_2O_3 nanoparticles in the amorphous Li–Si–P oxide matrix by the annealing and first discharging. Amorphous Li–Si–P oxides are often used as solid electrolytes in LIBs owing to their high Li^+ ion conductivity.[57–60] Therefore, the amorphous Li–Si–P oxide layer between the Fe_2O_3 nanoparticles promoted the fast diffusion of the Li^+ ions in the active material. For the unannealed sample, the nanocomposite structure was formed through the insertion reaction of Li^+ ions during the discharge processes.[35] However, owing to the nonuniform electrode reaction occurring in the LIBs, the nanocomposite structure formed in the unannealed sample was possibly nonuniform; some *L*-BIOX particles may have retained their original structures even after the initial discharging process. Therefore, unannealed *L*-BIOX was confirmed two diffusion pathways from the Warburg impedance, and showed slow lithium-ion diffusion. In contrast, the phase-separation reaction by annealing proceeds more uniformly than the electrode reaction in LIBs. Therefore, the annealed *L*-BIOX samples formed more uniform nanocomposite structures than the unannealed material. Hence, the *L*-BIOX sample annealed at 700 °C exhibited an excellent rate performance owing to its uniform nanocomposite structure, which consequently reduced the diffusion resistance of Li^+ ions.

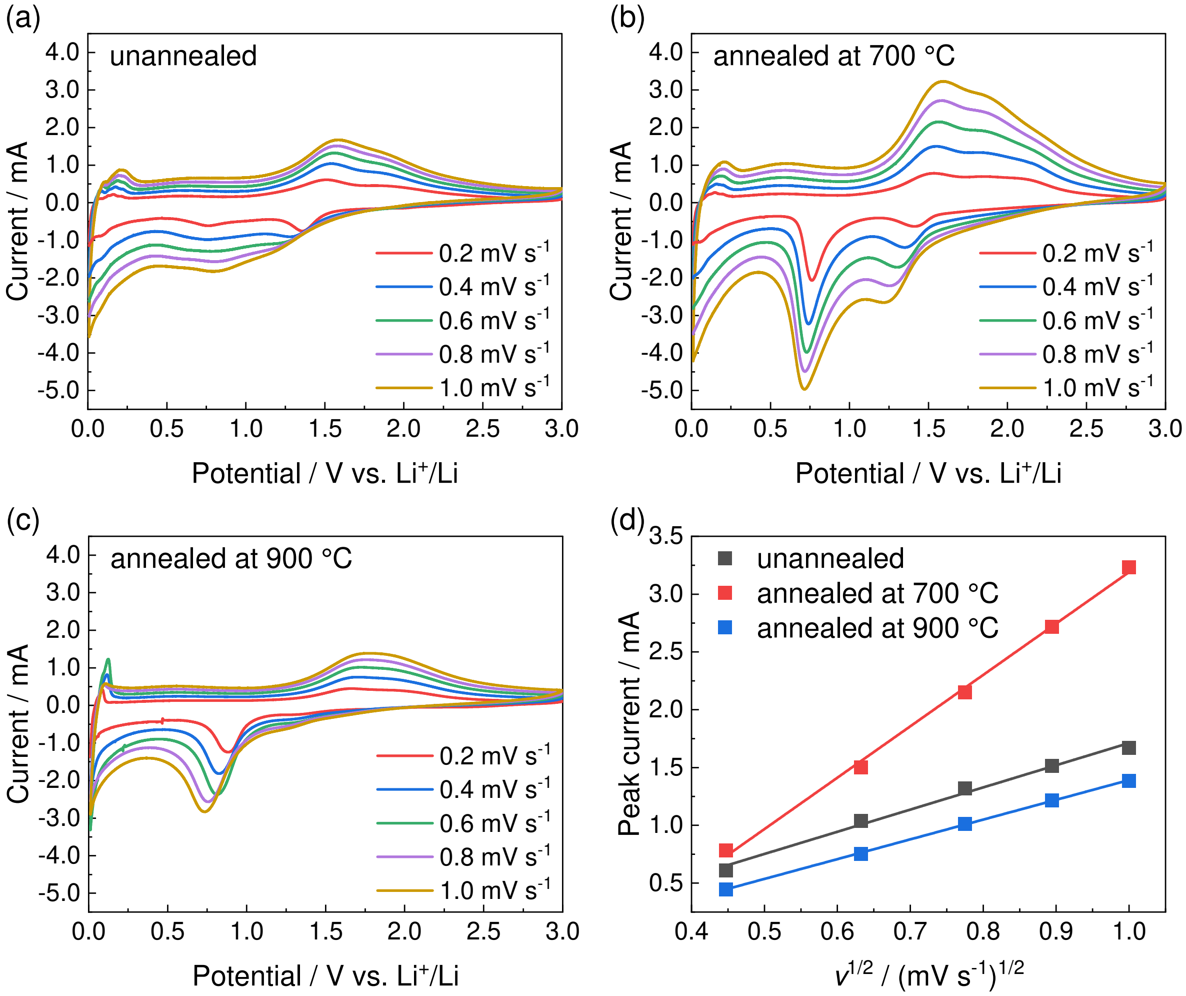

Figure 4. Cyclic voltammograms from 0.01–3 V vs. Li^+/Li at scan rate from 0.2 to 1.0 mV s^{-1} for the *L*-BIOX (a) unannealed and annealed at (b) 700 °C and (c) 900 °C. (d) The linear fitting of the peak current to square root of the scan rate for the *L*-BIOX unannealed and annealed at 700 °C.

Conclusion

In this study, the effect of nanocomposite structure of the *L*-BIOX samples formed by annealing at various temperature to the battery performance was revealed. The annealed *L*-BIOX samples at 300–700 °C exhibited higher rate performances than the unannealed material. In particular, the *L*-BIOX sample annealed at 700 °C exhibited a higher rate performance than the previously reported Fe_2O_3-based anode materials. From the analysis of the cyclic voltammograms, the calculated diffusion coefficient of the *L*-BIOX sample annealed at 700 °C was 3.48 times of that the unannealed material. The nanocomposite structure allowed the fast diffusion of Li^+ ions because the Li–Si–P oxide matrix functioned as fast diffusion path. The low diffusion coefficient in the unannealed *L*-BIOX sample was possibly due to the retention of its initial structure even after the discharge process. The nanocomposite structure in the unannealed *L*-BIOX sample was formed through the insertion reaction of Li^+ ions. However, the structure produced after the discharging process was possibly nonuniform because electrochemical reactions proceed in a nonuniform manner. This is in sharp contrast with the phase separation reaction achieved through annealing. Consequently, the nanocomposite structure of the *L*-BIOX sample annealed at 700 °C was more homogeneous than that of the unannealed material. The formation of a uniform nanocomposite structure led to the reduction in the diffusion resistance of the Li^+ ions in the active material, which consequently improved the rate performance of the electrode. This study provides significant insights to the development of novel Fe_2O_3-based anode nanomaterials for LIBs.

AUTHOR INFORMATION

Corresponding Author

Tatsuo Fujii – *Graduate School of Natural Science and Technology, Okayama University, Okayama 700-8530, Japan;* E-mail: tfujii@cc.okayama-u.ac.jp

Present Addresses

Hideki Hashimoto – *Department of Applied Chemistry, Kogakuin University, Nakano-machi 2665-1, Hachioji-shi, Tokyo 192-0015, Japan.*

ASSOCIATED CONTENT

Supporting information: Discharge/charge voltage profiles of all samples in cycle and rate performances evaluation test; Equivalent circuits diagram used for fitting the impedance spectra and fitting result of impedance spectra of *L*-BIOX unannealed and annealed for 700 °C.

Acknowledgement

I would like to thank Yasuo Takeda and Mikio Takano for useful discussions.

Reference

(1) Zubi, G.; Dufo-López, R.; Carvalho, M.; Pasaoglu, G. The Lithium-Ion Battery: State of the Art and Future Perspectives. *Renew. Sust. Energy Rev.* **2018**, *89*, 292–308. https://doi.org/10.1016/j.rser.2018.03.002.

(2) Dunn, B.; Kamath, H.; Tarascon, J.-M. Electrical Energy Storage for the Grid: A Battery of Choices. *Science* **2011**, *334*, 928–935. https://doi.org/10.1126/science.1212741.

(3) Yang, Z.; Zhang, J.; Kintner-Meyer, M. C. W.; Lu, X.; Choi, D.; Lemmon, J. P.; Liu, J. Electrochemical Energy Storage for Green Grid. *Chem. Rev.* **2011**, *111*, 3577–3613. https://doi.org/10.1021/cr100290v.

(4) Nitta, N.; Wu, F.; Lee, J. T.; Yushin, G. Li-Ion Battery Materials: Present and Future. *Mater. Today* **2015**, *18*, 252–264. https://doi.org/10.1016/J.MATTOD.2014.10.040.

(5) Goodenough, J. B.; Park, K.-S. The Li-Ion Rechargeable Battery: A Perspective. *J. Am. Chem. Soc.* **2013**, *135*, 1167–1176. https://doi.org/10.1021/ja3091438.

(6) Tarascon, J.-M.; Armand, M. Issues and Challenges Facing Rechargeable Lithium Batteries. *Nature* **2001**, *414*, 359–367. https://doi.org/10.1038/35104644.

(7) Yazami, R.; Zaghib, K.; Deschamps, M. Carbon Fibres and Natural Graphite as Negative Electrodes for Lithium Ion-Type Batteries. *J. Power Sources* **1994**, *52*, 55–59. https://doi.org/10.1016/0378-7753(94)01933-9.

(8) Manev, V.; Naidenov, I.; Puresheva, B.; Zlatilova, P.; Pistoia, G. Electrochemical Performance of Natural Brazilian Graphite as Anode Material for Lithium-Ion Rechargeable Cells. *J. Power Sources* **1995**, *55*, 211–215. https://doi.org/10.1016/0378-7753(95)02192-J.

(9) Kucinskis, G.; Bajars, G.; Kleperis, J. Graphene in Lithium Ion Battery Cathode Materials: A Review. *J. Power Sources* **2013**, *240*, 66–79. https://doi.org/10.1016/J.JPOWSOUR.2013.03.160.

(10) Xiang, F.; Hou, W.; Gu, X.; Wen, L.; Sun, Y.; Lu, W. One-Pot Synthesis of MnO-Loaded Mildly Expanded Graphite Composites as High-Performance Lithium-Ion Battery Anode Materials. *J. Alloys Compd.* **2022**, *897*, 163202. https://doi.org/10.1016/J.JALLCOM.2021.163202.

(11) Kim, H.; Choi, W.; Yoon, J.; Um, J. H.; Lee, W.; Kim, J.; Cabana, J.; Yoon, W.-S. Exploring Anomalous Charge Storage in Anode Materials for Next-Generation Li Rechargeable Batteries. *Chem. Rev.* **2020**, *120*, 6934–6976. https://doi.org/10.1021/acs.chemrev.9b00618.

(12) Jiang, J.; Li, Y.; Liu, J.; Huang, X.; Yuan, C.; Lou, X. W. Recent Advances in Metal Oxide-Based Electrode Architecture Design for Electrochemical Energy Storage. *Adv. Mater.* **2012**, *24*, 5166–5180. https://doi.org/10.1002/ADMA.201202146.

(13) Fang, S.; Bresser, D.; Passerini, S. Transition Metal Oxide Anodes for Electrochemical Energy Storage in Lithium- and Sodium-Ion Batteries. *Adv. Energy Mater.* **2020**, *10*, 1902485. https://doi.org/10.1002/AENM.201902485.

(14) Huang, Y.; Lin, Z.; Zheng, M.; Wang, T.; Yang, J.; Yuan, F.; Lu, X.; Liu, L.; Sun, D. Amorphous Fe_2O_3 Nanoshells Coated on Carbonized Bacterial Cellulose Nanofibers as a Flexible Anode for High-Performance Lithium Ion Batteries. *J. Power Sources* **2016**, *307*, 649–656. https://doi.org/10.1016/J.JPOWSOUR.2016.01.026.

(15) Liu, X.; Si, W.; Zhang, J.; Sun, X.; Deng, J.; Baunack, S.; Oswald, S.; Liu, L.; Yan, C.; Schmidt, O. G. Free-Standing Fe_2O_3 Nanomembranes Enabling Ultra-Long Cycling Life and High Rate Capability for Li-Ion Batteries. *Sci. Rep.* **2015**, *4*, 7452. https://doi.org/10.1038/srep07452.

(16) Cao, Y.; Yang, Y.; Ren, Z.; Jian, N.; Gao, M.; Wu, Y.; Zhu, M.; Pan, F.; Liu, Y.; Pan, H. A New Strategy to Effectively Suppress the Initial Capacity Fading of Iron Oxides by Reacting with $LiBH_4$. *Adv. Funct. Mater.* **2017**, *27*, 1700342. https://doi.org/10.1002/adfm.201700342.

(17) Yang, L.; Wu, Y.; Wu, Y.; Younas, W.; Jia, J.; Cao, C. Hierarchical Flower-like Fe_2O_3 Mesoporous Nanosheets with Superior Electrochemical Lithium Storage Performance. *J. Energy Storage* **2019**, *23*, 363–370. https://doi.org/10.1016/j.est.2019.04.003.

(18) Guo, W.; Sun, W.; Lv, L.-P.; Kong, S.; Wang, Y. Microwave-Assisted Morphology Evolution of Fe-Based Metal–Organic Frameworks and Their Derived Fe_2O_3 Nanostructures for Li-Ion Storage. *ACS Nano* **2017**, *11*, 4198–4205. https://doi.org/10.1021/acsnano.7b01152.

(19) Cheong, J. Y.; Koo, W.-T.; Kim, C.; Jung, J.-W.; Kim, I.-D. Feasible Defect Engineering by Employing Metal Organic Framework Templates into One-Dimensional Metal Oxides for Battery Applications. *ACS Appl. Mater. Inter.* **2018**, *10*, 20540–20549. https://doi.org/10.1021/acsami.8b04968.

(20) Zhou, Z.; Zhang, Q.; Sun, J.; He, B.; Guo, J.; Li, Q.; Li, C.; Xie, L.; Yao, Y. Metal–Organic Framework Derived Spindle-like Carbon Incorporated α-Fe_2O_3 Grown on Carbon Nanotube Fiber as Anodes for High-Performance Wearable Asymmetric Supercapacitors. *ACS Nano* **2018**, *12*, 9333–9341. https://doi.org/10.1021/acsnano.8b04336.

(21) Ma, Y.; Zhang, L.; Cai, Z.; Huang, X.; Ding, B.; Ahsan, Z.; Song, G.; Xu, Y.; Yang, W.; Wen, C. Study of TiO_2-Coated α-Fe_2O_3 Composites and the Oxygen-Defects Effect on the Application as the Anode Materials of High-Performance Li-Ion Batteries. *ACS Appl. Energy Mater.* **2020**, *3*, 11666–11673. https://doi.org/10.1021/acsaem.0c01661.

(22) Zhang, C.; Chen, Z.; Wang, H.; Nie, Y.; Yan, J. Porous Fe_2O_3 Nanoparticles as Lithium-Ion Battery Anode Materials. *ACS Appl. Nano Mater.* **2021**, *4*, 8744–8752. https://doi.org/10.1021/acsanm.1c01312.

(23) Xu, X.; Cao, R.; Jeong, S.; Cho, J. Spindle-like Mesoporous α-Fe_2O_3 Anode Material Prepared from MOF Template for High-Rate Lithium Batteries. *Nano Lett.* **2012**, *12*, 4988–4991.

(24) Hashimoto, H.; Kobayashi, G.; Sakuma, R.; Fujii, T.; Hayashi, N.; Suzuki, T.; Kanno, R.; Takano, M.; Takada, J. Bacterial Nanometric Amorphous Fe-Based Oxide: A Potential Lithium-Ion Battery Anode Material. *ACS Appl. Mater. Inter.* **2014**, *6*, 5374–5378.

(25) Sakuma, R.; Hashimoto, H.; Kobayashi, G.; Fujii, T.; Nakanishi, M.; Kanno, R.; Takano, M.; Takada, J. High-Rate Performance of a Bacterial Iron-Oxide Electrode Material for Lithium-Ion Battery. *Mater. Lett.* **2015**, *139*, 414–417.

(26) Hashimoto, H.; Fujii, T.; Kohara, S.; Asaoka, H.; Kusano, Y.; Ikeda, Y.; Nakanishi, M.; Benino, Y.; Nanba, T.; Takada, J. Amorphous Structure of Iron Oxide of Bacterial Origin. *Mater. Chem. Phys.* **2012**, *137*, 571–575.

(27) Furusawa, H.; Konishi, R.; Mori, D.; Horino, H.; Horiba, T.; Takeda, Y.; Takada, J.; Yamamoto, O.; Imanishi, N. Biogenous Iron Oxide (L-BIOX) as a High Capacity Anode Material for Lithium Ion Batteries. *Electrochim. Acta* **2018**, *281*, 227–236.

(28) Hashimoto, H.; Asaoka, H.; Nakano, T.; Kusano, Y.; Ishihara, H.; Ikeda, Y.; Nakanishi, M.; Fujii, T.; Yokoyama, T.; Horiishi, N. et al. Preparation, Microstructure, and Color Tone of Microtubule Material Composed of Hematite/Amorphous-Silicate Nanocomposite from Iron Oxide of Bacterial Origin. *Dyes Pigments* **2012**, *95*, 639–643.

(29) Hashimoto, H.; Fujii, T.; Kohara, S.; Nakanishi, K.; Yogi, C.; Peterlik, H.; Nakanishi, M.; Takada, J. Structural Transformations of Heat-Treated Bacterial Iron Oxide. *Mater. Chem. Phys.* **2015**, *155*, 67–75.

(30) Seehra, M. S.; Roy, P.; Raman, A.; Manivannan, A. Structural Investigations of Synthetic Ferrihydrite Nanoparticles Doped with Si. *Solid State Commun.* **2004**, *130*, 597–601.

(31) Jitianu, A.; Crisan, M.; Meghea, A.; Rau, I.; Zaharescu, M. Influence of the Silica Based Matrix on the Formation of Iron Oxide Nanoparticles in the Fe_2O_3–SiO_2 System, Obtained by Sol–Gel Method. *J. Mater. Chem.* **2002**, *12*, 1401–1407.

(32) Daou, T. J.; Pourroy, G.; Bégin-Colin, S.; Grenèche, J. M.; Ulhaq-Bouillet, C.; Legaré, P.; Bernhardt, P.; Leuvrey, C.; Rogez, G. Hydrothermal Synthesis of Monodisperse Magnetite Nanoparticles. *Chem. Mater.* **2006**, *18*, 4399–4404.

(33) Scarano, D.; Zecchina, A.; Bordiga, S.; Geobaldo, F.; Spoto, G.; Petrini, G.; Leofanti, G.; Padovan, M.; Tozzola, G. Fourier-Transform Infrared and Raman Spectra of Pure and Al-, B-, Ti- and Fe-Substituted Silicalites: Stretching-Mode Region. *J. Chem. Soc., Faraday Trans.* **1993**, *89*, 4123–4130.

(34) Tran, T. N.; Pham, T. V. A.; Le, M. L. P.; Nguyen, T. P. T.; Tran, V. M. Synthesis of Amorphous Silica and Sulfonic Acid Functionalized Silica Used as Reinforced Phase for Polymer Electrolyte Membrane. *Adv. Nat. Sci.: Nanosci. Nanotechnol.* **2013**, *4*, 045007.

(35) Hashimoto, H.; Ukita, M.; Sakuma, R.; Nakanishi, M.; Fujii, T.; Imanishi, N.; Takada, J. Bio-Inspired 2-Line Ferrihydrite as a High-Capacity and High-Rate-Capability Anode Material for Lithium-Ion Batteries. *J. Power Sources* **2016**, *328*, 503–509.

(36) Hashimoto, H.; Nishiyama, Y.; Ukita, M.; Sakuma, R.; Nakanishi, M.; Fujii, T.; Takada, J. Lithium Storage Properties of a Bioinspired 2-Line Ferrihydrite: A Silicon-Doped, Nanometric, and Amorphous Iron Oxyhydroxide. *Inorg. Chem.* **2015**, *54*, 7593–7599.

(37) Kang, E.; Jung, Y. S.; Cavanagh, A. S.; Kim, G. H.; George, S. M.; Dillon, A. C.; Kim, J. K.; Lee, J. Fe_3O_4 Nanoparticles Confined in Mesocellular Carbon Foam for High Performance Anode Materials for Lithium-Ion Batteries. *Adv. Funct. Mater.* **2011**, *21*, 2430–2438.

(38) Ban, C.; Wu, Z.; Gillaspie, D. T.; Chen, L.; Yan, F.; Blackburn, J. L.; Dillon, A. C. Nanostructured Fe_3O_4/SWNT Electrode: Binder-Free and High-Rate Li-Ion Anode. *Adv. Mater.* **2010**, *22*, E145–E149.

(39) Yang, S.; Sun, Y.; Chen, L.; Hernandez, Y.; Feng, X.; Müllen, K. Porous Iron Oxide Ribbons Grown on Graphene for High-Performance Lithium Storage. *Sci. Rep.* **2012**, *2*, 427.

(40) Wu, C.; Yin, P.; Zhu, X.; OuYang, C.; Xie, Y. Synthesis of Hematite (α-Fe_2O_3) Nanorods: Diameter-Size and Shape Effects on Their Applications in Magnetism, Lithium Ion Battery, and Gas Sensors. *J. Phys. Chem. B* **2006**, *110*, 17806–17812.

(41) Yang, S.; Feng, X.; Müllen, K. Sandwich-Like, Graphene-Based Titania Nanosheets with High Surface Area for Fast Lithium Storage. *Adv. Mater.* **2011**, *23*, 3575–3579.

(42) Zhu, X.; Zhu, Y.; Murali, S.; Stoller, M. D.; Ruoff, R. S. Nanostructured Reduced Graphene Oxide/Fe_2O_3 Composite as a High-Performance Anode Material for Lithium Ion Batteries. *ACS Nano* **2011**, *5*, 3333–3338.

(43) Sun, H.; Xin, G.; Hu, T.; Yu, M.; Shao, D.; Sun, X.; Lian, J. High-Rate Lithiation-Induced Reactivation of Mesoporous Hollow Spheres for Long-Lived Lithium-Ion Batteries. *Nat. Commun.* **2014**, *5* (1), 4526.

(44) Palanisamy, K.; Kim, Y.; Kim, H.; Kim, J. M.; Yoon, W.-S. Self-Assembled Porous MoO_2/Graphene Microspheres towards High Performance Anodes for Lithium Ion Batteries. *J. Power Sources* **2015**, *275*, 351–361.

(45) Lian, Q.; Zhou, G.; Liu, J.; Wu, C.; Wei, W.; Chen, L.; Li, C. Extrinsic Pseudocapacitve Li-Ion Storage of SnS Anode via Lithiation-Induced Structural Optimization on Cycling. *J. Power Sources* **2017**, *366*, 1–8.

(46) Luo, J.; Liu, J.; Zeng, Z.; Ng, C. F.; Ma, L.; Zhang, H.; Lin, J.; Shen, Z.; Fan, H. J. Three-Dimensional Graphene Foam Supported Fe_3O_4 Lithium Battery Anodes with Long Cycle Life and High Rate Capability. *Nano Lett.* **2013**, *13* (12), 6136–6143.

(47) Lv, X.; Deng, J.; Wang, B.; Zhong, J.; Sham, T.-K.; Sun, X.; Sun, X. γ-Fe_2O_3@CNTs Anode Materials for Lithium Ion Batteries Investigated by Electron Energy Loss Spectroscopy. *Chem. Mater.* **2017**, *29* (8), 3499–3506.

(48) Hyun Um, J.; Palanisamy, K.; Jeong, M.; Kim, H.; Yoon, W.-S. Phase Dynamics on Conversion-Reaction-Based Tin-Doped Ferrite Anode for Next-Generation Lithium Batteries. *ACS Nano* **2019**, *13* (5), 5674–5685.

(49) Li, X.; Qiao, L.; Li, D.; Wang, X.; Xie, W.; He, D. Three-Dimensional Network Structured α-Fe_2O_3 Made from a Stainless Steel Plate as a High-Performance Electrode for Lithium Ion Batteries. *J. Mater. Chem. A* **2013**, *1* (21), 6400–6406.

(50) Tang, J.; Zavala Lugo, C. E.; Acuña Guzmán, S. F.; Daniel, G.; Kessler, V. G.; Seisenbaeva, G. A.; Pol, V. G. Pushing the Theoretical Capacity Limits of Iron Oxide Anodes: Capacity Rise of γ-Fe_2O_3 Nanoparticles in Lithium-Ion Batteries. *J. Mater. Chem. A* **2016**, *4* (46), 18107–18115.

(51) Tian, R.; Park, S. H.; King, P. J.; Cunningham, G.; Coelho, J.; Nicolosi, V.; Coleman, J. N. Quantifying the Factors Limiting Rate Performance in Battery Electrodes. *Nat. Commun.* **2019**, *10*, 1993.

(52) Ye, J.; C. Baumgaertel, A.; Morris Wang, Y.; Biener, J.; M. Biener, M. Structural Optimization of 3D Porous Electrodes for High-Rate Performance Lithium Ion Batteries. *ACS Nano* **2014**, *9*, 2194–2202.

(53) Zhang, H.; Yu, X.; Braun, P. v. Three-Dimensional Bicontinuous Ultrafast-Charge and-Discharge Bulk Battery Electrodes. *Nat. Nanotech.* **2011**, *6*, 277–281.

(54) Choi, W.; Shin, H. C.; Kim, J. M.; Choi, J. Y.; Yoon, W. S. Modeling and Applications of Electrochemical Impedance Spectroscopy (EIS) for Lithium-Ion Batteries. J. *Electrochem. Sci. Technol.* **2020**, *11*, 1–13.

(55) Osaka, T.; Nara, H.; Mukoyama, D.; Yokoshima, T. New Analysis of Electrochemical Impedance Spectroscopy for Lithium-Ion Batteries. *Journal of Electrochemical Science and Technology* **2013**, *4* (4), 157–162.

(56) Ganguly, D.; Piriya, A.; Ghosh, A.; Ramaprabhu, S. Magnetic Field Assisted High Capacity Durable Li-Ion Battery Using Magnetic α-Fe_2O_3 Nanoparticles Decorated Expired Drug Derived N-Doped Carbon Anode. *Sci. Rep.* **2020**, *10*, 1-10.

(57) Chen, C.; Jiang, M.; Zhou, T.; Raijmakers, L.; Vezhlev, E.; Wu, B.; Schülli, T. U.; Danilov, D. L.; Wei, Y.; Eichel, R. A. et al. Interface Aspects in All-Solid-State Li-Based Batteries Reviewed. *Adv. Energy Mater.* **2021**, **11**, 2003939.

(58) Deng, Y.; Eames, C.; Chotard, J.-N.; Lalère, F.; Seznec, V.; Emge, S.; Pecher, O.; Grey, C. P.; Masquelier, C.; Islam, M. S. Structural and Mechanistic Insights into Fast Lithium-Ion Conduction in Li_4SiO_4–Li_3PO_4 Solid Electrolytes. *J. Am. Chem. Soc.* **2015**, *137*, 9136–9145.

(59) Sakurai, Y.; Sakuda, A.; Hayashi, A.; Tatsumisago, M. Preparation of Amorphous Li_4SiO_4–Li_3PO_4 Thin Films by Pulsed Laser Deposition for All-Solid-State Lithium Secondary Batteries. *Solid State Ionics* **2011**, *182*, 59–63.

(60) Bates, J. B.; Dudney, N. J.; Gruzalski, G. R.; Zuhr, R. A.; Choudhury, A.; Luck, C. F.; Robertson, J. D. Electrical Properties of Amorphous Lithium Electrolyte Thin Films. *Solid State Ionics* **1992**, *53–56*, 647–654.

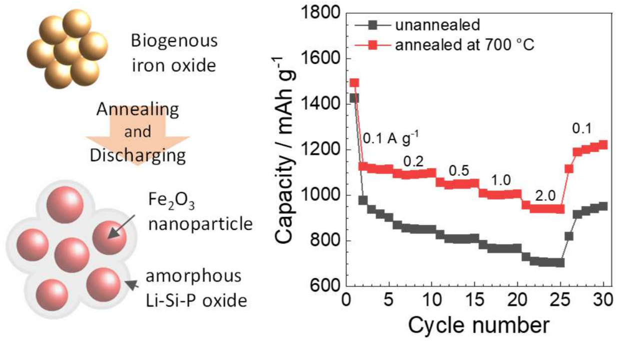
Biogenous iron oxide
Annealing and Discharging
Fe_2O_3 nanoparticle
amorphous Li-Si-P oxide
unannealed
annealed at 700 °C
0.1 A g^{-1}
0.2
0.5
1.0
2.0
0.1
Capacity / mAh g^{-1}
600
800
1000
1200
1400
1600
1800
0
5
10
15
20
25
30
Cycle number

TOC Graphic